# SUPPLEMENTARY MATERIAL

## Fitting Membrane Profiles to Experimental Data

We selected membrane profiles from the experimental study by Kukulski et al. [8] to estimate a mean membrane profile during the initial stage of endocytosis. Profiles that had invaginations of 11 nm or less and a clear peak were initially collected. These profiles were labeled by the authors of the experimental study [8] as 120, 1013, 1014, 1017, 1018, 1021, and 1023. The maximum invaginations of each profile are listed in Table S1. Three of these profiles are clearly symmetrical (profiles 120, 1014, and 1017), and this set of profiles is referred to as the "Symmetric Selection" set in Table S1. Of the remaining profiles, one side or the other (from the peak displacement) fits the general shape of the Symmetric Selection set. We refer to the set of profiles including both the Symmetric Selection set and the partial profiles as the "Outlier Rejection" set. Table S1 indicates which sides of the profiles are included in the Outlier Rejection set.

TABLE S1: Curves from the experimental study by Kukulski et al. [8] that have less than the maximum invagination of 11 nm and have a clear axis of symmetry. Profile numbers are those of Ref. [8]. The maximum displacement of the invagination at the axis of symmetry is given for each profile. For the "Outlier Rejection" set, the sides included in the averaged profile are indicated. The "Symmetric Selection" set includes both sides of the selected profiles.

| Profile | Maximum Disp. [nm] | Outlier Rejection | Symmetric Selection |
|---|---|---|---|
| 120 | 7.5 | left & right | left & right |
| 1013 | 6.9 | left | |
| 1014 | 6.7 | left & right | left & right |
| 1017 | 9.2 | left & right | left & right |
| 1018 | 10.4 | left | |
| 1021 | 10.8 | left | |
| 1023 | 10.2 | right | |

To find a mean profile, the profiles are flipped vertically to follow the convention shown in Fig. 2b, and the axis of rotation is taken to be the maximum displacement point. Before averaging, profiles are normalized by their respective peak invaginations and interpolated using a cubic spline along a common grid. The invagination depth of the resulting mean profiles, shown in Fig. S1a, is the mean depth of the original profiles. The mean profiles from the Outlier Rejection and Symmetric Selection sets are similar.

## Sensitivity Studies

In this section, we discuss a number of parameter studies we performed to assess the effects of parameters on the growth simulations and the estimated actin force.

1. **Fitting of Membrane Profile.** Figure S1b shows a Gaussian fit (see Eq. 7) of the two mean profiles from Fig. S1a. The Symmetric Selection set results in a displacement profile with a slightly narrower dimple. Note that the fitting parameter $B$ from Eq. 7, which does not affect the curvature, has been discarded in both cases. The resulting force densities $-(f_W + P_0)$ from the FE simulations for both the Outlier Rejection and Symmetric Selection sets are compared in Fig. S1c. The force density from the Symmetric Selection set is about 4 nm narrower at the point $R'_W$ (defined here as the location where $f_W + P_0 = 0$) than for the Outlier Rejection set. This indicates that $R'_W$ is not particularly sensitive to the selection criteria of the membrane profiles.

   In the spatial domain ($r$ and $z$), we fit the mean displacement profile from Fig. 2c using a Gaussian function. A Gaussian curve provides a continuous fit to the full radius of the actin patch (100 nm or more). Since the mean data from Fig. 2 is continuous to about 46 nm, a Gaussian fit is more convenient than a polynomial fit for the full actin patch. We chose a polynomial fit in the arc length coordinates ($s$ and $\psi(s)$) for convenience in

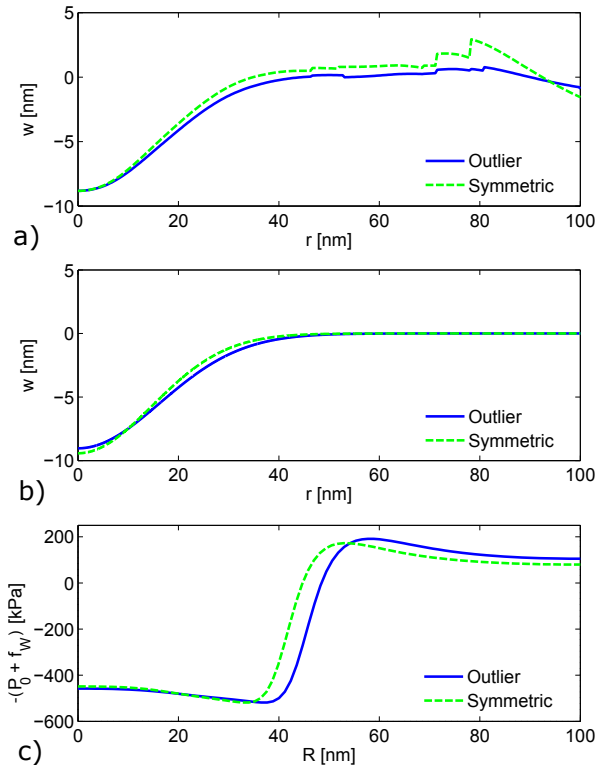


FIG. S1: Comparisons of a) the mean profiles, b) Gaussian fits of the mean profiles, and c) the resulting wall reaction forces using the displacement sets defined in Table S1. The curves found using the "Outlier Rejection" displacement sets are represented by solid lines, and those found using the "Symmetric Selection" displacement sets are represented by dashed lines.

implementing the boundary conditions for Eq. 2. For the polynomial fit, the BCs could be met by constraining the odd terms to vanish. In order to compare these two fits, we transformed the polynomial fit into the spatial domain by numerically integrating the following two relationships:

$$r = \int_0^s \cos\left[\psi(s)\right]\, \mathrm{d}s \quad \text{and} \tag{S1}$$

$$z = -\int_s^S \sin\left[\psi(s)\right]\, \mathrm{d}s + z_0\,, \tag{S2}$$

where $S$ is the maximum curve length ($S \approx 46$ nm). For the integration constant $z_0$ in Eq. S2, we chose the parameter $A$ from the Gaussian fit in the spatial domain (see Eq. 7). Figure S2 provides a comparison of the Gaussian and integrated polynomial fits in the spatial domain. The comparison between the two fits is quite close, and the choice of two different fitting functions for the spatial and arc length coordinates appears reasonable.

## 2. Growth Parameters

For a numerical assessment of the agreement between the estimated and simulated actin forces, we use a

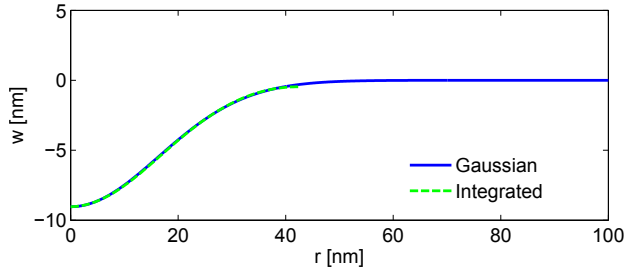


FIG. S2: Comparison of the Gaussian fit of the mean displacement profile (see Fig. 2c) and the integrated polynomial fit of the mean displacement profile in the arc length domain. The integration of the polynomial fit is only continuous to a radius of $r \approx 46$ nm.

normalized, absolute-mean error $E_A$. This error is defined as

$$E_A = \frac{\int_0^{R_A} \left| f_A^{sim}(r) - f_A(r) \right| 2\pi r \, \mathrm{d}r}{\int_0^{R_A} \left| f_A(r) \right| 2\pi r \, \mathrm{d}r}, \tag{S3}$$

where $f_A^{sim}(r)$ is the simulated actin force, $f_A(r)$ is the estimated actin force, and $R_A$ is the radius of the actin patch.

TABLE S2: Effect of growth and material parameters on quality of fit. $R_A$ is the radius of the actin network, $\alpha$ determines the nonlinearity in the Fung model, and $Z_p$ is the width of the growing region of the actin network. For each set of parameters, the error $E_A$ between the simulated and estimated actin force is given. The error $E_A$ is the normalized, absolute-mean error integrated over the surface of the actin as defined by Eq. S3. Normalized forces are used to calculate $E_A$ for simulations with linear strains, and the full magnitude forces are used to calculate $E_A$ for simulations with nonlinear strains.

| Section in Text | Parameter | $E_A$ | |
|---|---|---|---|
| | | Linear Strains | Nonlinear Strains |
| 2a | $R_A = 100$ nm | 0.05 | 0.11 |
| | $R_A = 150$ nm | 0.04 | 0.11 |
| | $R_A = 200$ nm | 0.04 | - |
| 2b | $\alpha = 0.001$ | 0.05 | 0.12 |
| | $\alpha = 0.01$ | 0.05 | 0.11 |
| | $\alpha = 0.02$ | 0.05 | 0.11 |
| 2c | $Z_p = 20$ nm | 0.05 | 0.16 |
| | $Z_p = 25$ nm | 0.05 | 0.11 |
| | $Z_p = 30$ nm | 0.04 | 0.12 |

(a) **Effect of the Actin Network Radius on Calculated Growth Forces.** We tried increasing the actin patch radius to 150 nm. The shape of the calculated force profile was similar to the 100 nm baseline case, as shown in Fig. S3. The compressive force density is lower for the actin radius of $R_A = 150$ nm, as expected for the larger area. Table S2 shows that the actin radius has almost no effect on the agreement between simulated and estimated actin forces for simulations with linear or nonlinear strains.

(b) **Effect of the Parameter $\alpha$ in the Fung model.** We ran growth simulations with $\alpha$ taking the values 0.001, 0.01, and 0.02, using the same growth profiles as in the baseline simulations. The change in $\alpha$ resulted in no appreciable difference in the simulated actin force density $f_A$. Table S2 shows no significant changes in agreement between simulated and estimated actin forces due to changes in $\alpha$.

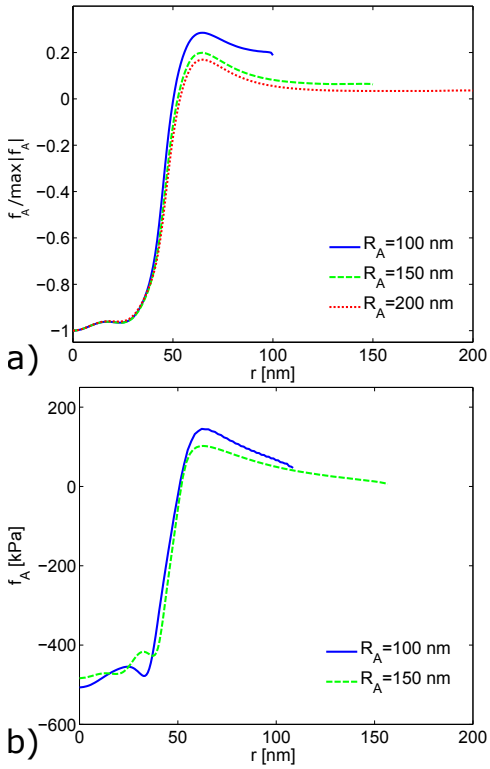


FIG. S3: Comparison of actin force $f_A$ obtained from growth simulations for increasing radii of the actin patch. a) Normalized actin forces for linear strains. b) Full-magnitude comparisons of actin forces for nonlinear strains.

(c) **Effect of the Polymerization Region Thickness.** We ran growth simulations with polymerization region thicknesses of $Z_p$ = 20, 25, and 30 nm, again using growth profiles from the baseline simulations. The differences in $f_A$ for $Z_p$ = 25 and 30 nm were insignificant as is apparent from Fig. S4 and Table S2. As seen in Fig. S4, the differences in $f_A$ between the simulations with $Z_p$ = 20 and 25 nm were more noticeable. Table S2 also indicates a poorer fit between simulated and estimated actin force for $Z_p$ = 20 nm. Thus the nonlinear-strain growth model is sensitive to $Z_p$ parameters below 25 nm, but it is not particular sensitive to larger values of $Z_p$.

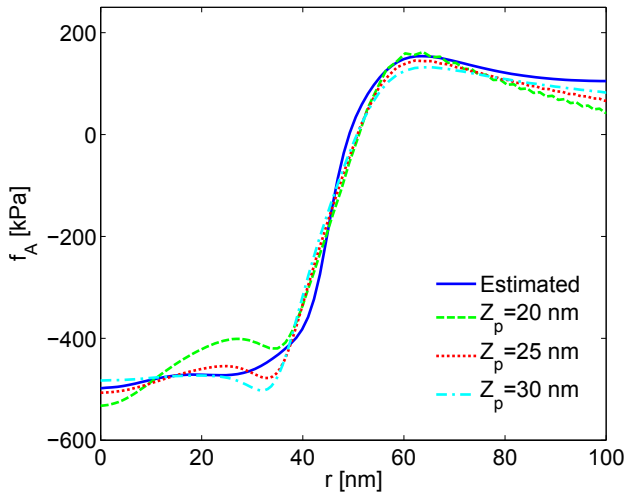


FIG. S4: Comparison of actin force $f_A$ from actin growth simulations for nonlinear strains and polymerization region thicknesses of $Z_p$ = 20, 25, and 30 nm. The corrected growth profile $g(r)$ from Fig. 9a was used for all three simulations. "Estimated" denotes force profile obtained from experimental data.

(d) **Effect of Shape of Growth Profile.** Finally, we simulated the actin force density generated by several arbitrarily chosen growth profiles shown in Fig. S5a. We tried several parameters for the profile defined in Eq. 23 and a fitted profile based on our previous work [16]:

$$g(r) = \left[\frac{1}{\pi}\tan^{-1}\left(\frac{r - r_0}{0.1 r_0}\right) + \frac{1}{2}\right]^2 , \tag{S4}$$

It is clear that the different forms and parameters generate substantial differences in the calculated force densities. Thus the calculated actin force density is sensitive to the form and width of the growth profile. Therefore, a growth profile that generates the correct actin force density is likely to be reasonably correct.

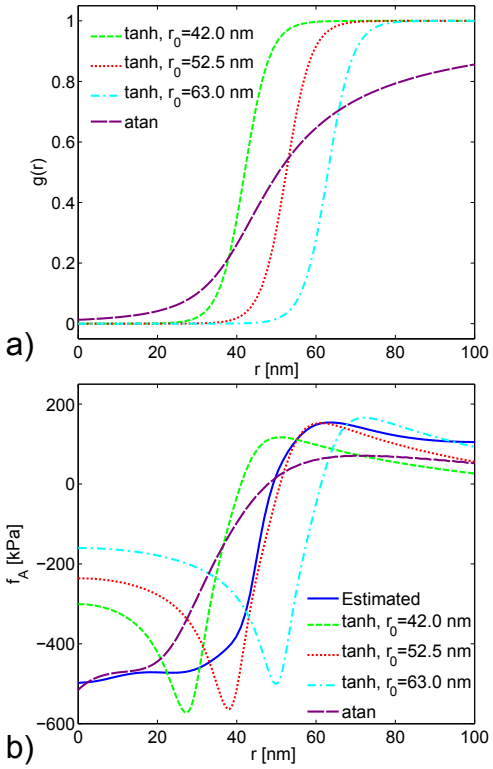


FIG. S5: a) Growth profiles used for simulating actin forces. The tanh curves are defined by Eq. 23 with parameter values of $\eta = 0.16$ nm$^{-1}$ and $r_0 = 42.0$, 52.5, and 63.0 nm. The atan curve is based on Eq. S4 with $r_0 = 39.5$ nm, and $0.1r_0$ is replaced with a fitted value of 14.5 nm. b) Comparison of simulated actin force $f_A$ using the growth profiles from Fig. a) (broken lines), and the actin force density estimated from experiments (solid line).

## 3. Cell Wall Parameters, Turgor Pressure and Geometry

(a) **Effect of Mechanical Model of Cell Wall.** We modeled the cell wall as both a continuous material (using FE simulation; see Fig. 6) and with a linear-spring bed model (not shown), and calculated $f_W$ using each model. The spring bed model assumes that the displacement of the cell wall at any particular point along the wall is independent the displacements at other points. A comparison of the force $-(f_W + P_0)$ between both models for a turgor pressure of $P_0 = 0.5$ MPa is shown in Fig. S6a. The sharp transition that occurs at $r \approx 38$ nm for the spring bed model is the location at which the membrane separates from the cell wall. The transition is smooth for the continuous material model because displacements at any particular point along the cell wall impact the displacements at other points.

The two cell wall models represent extremes in treating the cell wall as a continuous or spatially uncoupled material. We expect that the behavior of the cell wall to fall somewhere within these two approaches. To estimate the sensitivity to the mechanical properties assumed for the cell wall, we performed a sensitivity analysis using both cell wall models and three turgor pressures. We used a error propagation approach [49]

to estimate the sensitivity to the two types of models. We define the standard error or sensitivity at a given $r$ as

$$\alpha_T^2(r) = \sum_{n=1}^{N} \left| f_W^{\mathrm{FE}}(r, P_n) - f_W^{\mathrm{Spring}}(r, P_n) \right|^2 \left( \frac{P_0}{P_n} \right)^2, \tag{S5}$$

where $P_n = 0.25$, 0.50, and 0.75 MPa are the three turgor pressures in the study, and $N = 3$ for three pressures. Figure S6 shows the force $(f_W + P_0) \pm \alpha_T$ for $P_0 = 0.5$ MPa. The largest sensitivities tend to occur at the transitions at $r \approx 38$ and $r \approx 58$ which are the locations where the continuous assumption makes the largest impact. The sensitivity of $R'_W$ to the cell wall model is less than 6 nm. The term $R'_W$ is defined here as the location at which $f_W + P_0 = 0$, and is expected to be the location where the membrane separates from the cell wall. This indicates that the location at which the membrane separates from the cell wall is not particularly sensitive to the cell wall model chosen in the analysis.

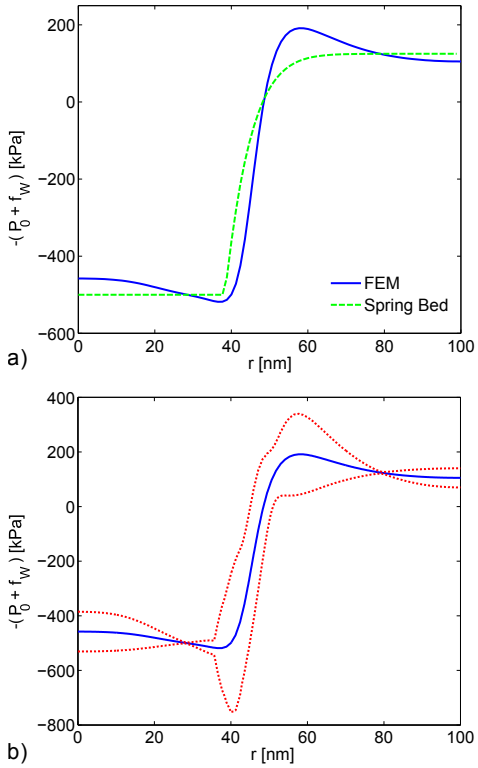


FIG. S6: a) Comparison between the cell wall reaction force and turgor pressure $(f_W + P_0)$ using elastic continuum (solid line) and linear-spring bed (dashed line) models of the cell wall. The turgor pressure in both simulations was $P_0 = 0.5$ MPa. b) Sensitivity analysis comparing the continuum and linear-spring bed cell wall models. The forces $f_W + P_0$ from the continuum model with $P_0 = 0.5$ MPa (solid line) and $(f_W + P_0) \pm \alpha_T$ (dotted lines) are shown. The sensitivity $\alpha_T$ is calculated from Eq. S5.

(b) **Effect of Poisson's Ratio.** In addition to comparing the different cell wall models, we also performed a study changing the Poisson's ratio in the continuum model of the cell wall. The baseline Poisson's ratio of $\nu = 0.49$ assumes that the cell wall is nearly incompressible. For a turgor pressure of $P_0 = 0.5$, we ran additional FE simulations for Poisson's ratios of $\nu = 0$ and 0.3. For all three cases, the actin force $f_A$ was nearly identical. We also calculated the pulling force $F_A$ and location $R_W$ where $f_A$ crosses from positive to negative. For all of the following cell wall parameter studies we define the pulling force as the total actin force, $f_A$, integrated over the area from $r = 0$ to $r = R_W$. Table S3 shows only small variations in $F_A$ and $R_W$ due to large changes in the Poisson's ratio. Based on these results, the main results of the continuum mechanics model of the cell wall are not sensitive to Poisson's ratio.

(c) **Effect of Young's Modulus.** We varied the Young's Modulus $E_W$ of the cell wall to assess the effect on both $F_A$ and $R_W$. Table S3 shows $F_A$ and $R_W$ for both the continuum and linear-spring bed models of the

cell wall with Young's Moduli of $E = 1/4 \times 110$, $1/2 \times 110$, 110, and $2 \times 110$ MPa. Based on this study, neither $F_A$ nor $R_W$ are particularly sensitive to the cell wall Young's modulus.

TABLE S3: Sensitivity of results to the cell wall Poisson's ratio $\nu_W$, cell wall Young's modulus $E_W$, and actin network radius $R_A$. The pulling force $F_A$ is the total actin force required to initiate endocytosis, and is calculated by integrating the force $f_A$ from $r = 0$ to $R_W$. $R_W$ is defined as the location where $f_A = 0$. Note that the spring bed model results do not include $f_M$ or $f_{CGP}$, and this model has no Poisson's ratio by definition.

| Section in Text | Parameter | $F_A$ [pN] | | $R_W$ [nm] | |
|---|---|---|---|---|---|
| | | Continuum | Spring Bed | Continuum | Spring Bed |
| 3b | $\nu_W = 0.0$ | 2800 | - | 47 | - |
| | $\nu_W = 0.3$ | 2700 | - | 46 | - |
| | $\nu_W = 0.49$ | 2800 | - | 48 | - |
| 3c | $E_W = 0.25 \times 110$ MPa | 2100 | 1800 | 42 | 43 |
| | $E_W = 0.5 \times 110$ MPa | 2500 | 2300 | 46 | 46 |
| | $E_W = 1.0 \times 110$ MPa | 2800 | 2800 | 48 | 48 |
| | $E_W = 2.0 \times 110$ MPa | 3000 | 3300 | 51 | 51 |
| 3d | $R_A = 100$ nm | 2800 | 2800 | 48 | 48 |
| | $R_A = 150$ nm | 2900 | 3000 | 51 | 53 |
| | $R_A = 200$ nm | 3000 | 3100 | 53 | 56 |

(d) **Effect of Actin Network Radius on on Force Profile Obtained from Experiments.** The required actin force densities $f_A$ calculated for the actin network radii of $R_A = 100$, 150, and 200 nm are shown in Fig. S7. Table S3 shows the corresponding values of $F_A$ and $R_W$ for both the continuum and linear-spring models for all three radii. The continuum model is insensitive to the width of the actin network, with almost no change in $F_A$ or $R_W$ for large changes in $R_A$. The total pulling force $F_A$ for the linear-spring bed model is also insensitive to changes in actin network radius. The radius $R_W$ in the spring bed model does vary for different actin radii. However, with a maximum change of 8 nm for a 300% increase in actin network area, this model does not appear to be particularly sensitive to the actin network radius.

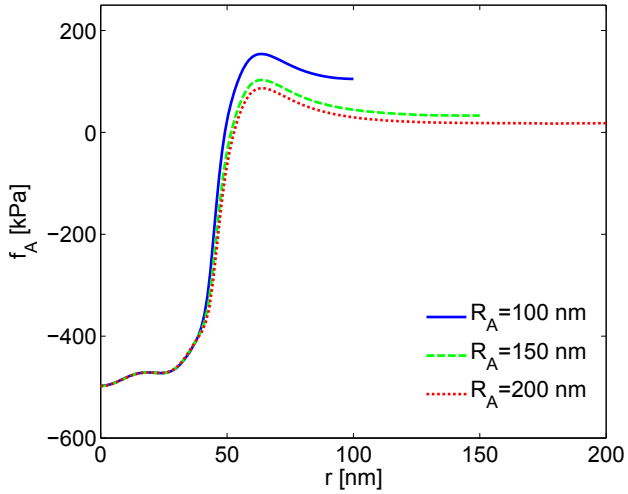


FIG. S7: Comparison of actin force profiles $f_A$ estimated from experiments for increasing radii of the actin network. The model from Fig. 4 was used to estimate the actin force for $R_A = 100$, 150 and 200 nm with a matching cell wall and membrane radius in each case.

(e) **Effect of Turgor Pressure**

The turgor pressure study summarized in Table S4 is discussed in the main text describing the continuum model of the cell wall. The results for the spring bed model are similar.

TABLE S4: Effects of turgor pressure on actin force $f_A$ and force crossover radius $R_W$. The pulling force $F_A$ is the total force required to initiate endocytosis, and is calculated by integrating the force $f_A$ from $r = 0$ to $r = R_W$. The spring bed model results do not include $f_M$ or $f_{CGP}$.

| $P_0$ [MPa] | $F_A$ [pN] | | $R_W$ [nm] | |
|---|---|---|---|---|
| | Continuum | Spring Bed | Continuum | Spring Bed |
| 0.25 | 1500 | 1700 | 53 | 51 |
| 0.5 | 2800 | 2800 | 48 | 48 |
| 1.0 | 5000 | 4600 | 45 | 45 |
| 2.0 | 8000 | 7200 | 41 | 42 |

4. Membrane and CGP Parameters

(a) **CGP Bending Modulus.** To observe the effect of changes in the CGP bending modulus on the actin force obtained from the growth simulations, we calculated the total actin force for several bending moduli: $\kappa_{CGP} = 20k_BT$, $285k_BT$, and $500k_BT$. Figure S8 shows that for a small bending modulus comparable to the bare membrane bending modulus $\kappa_{CGP} = 20k_BT$, the CGP continue to generate a relatively small force. On the other hand, nearly doubling the CGP bending modulus to $\kappa_{CGP} = 500k_BT$ results in a noticeably more rounded actin force density. Further increases in CGP bending modulus result in an actin force that is no longer smooth at the transition point at $s_0 = 46$ nm. Table S5 shows that the changes in CGP bending modulus have a minimal effect on both $F_A$ and $R_W$. For all membrane and CGP parameter studies we define the pulling force as the total actin force $f_A$, integrated over the area from $r = 0$ to $r = R_W$, where $R_W$ is the radial position at which $f_A = 0$. On the whole, the results are not strongly sensitive to changes in $\kappa_{CGP}$.

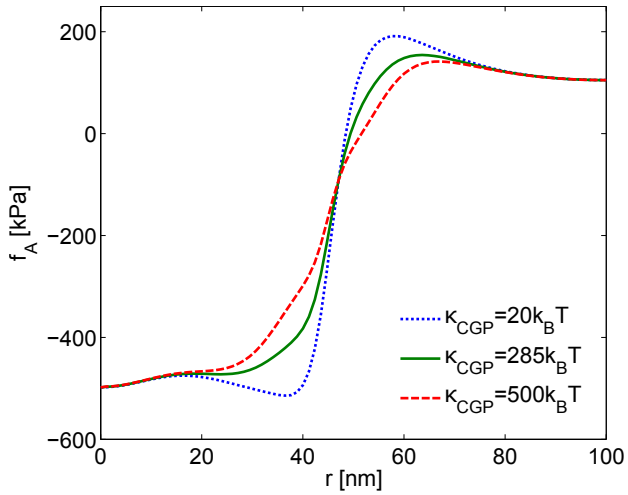


FIG. S8: Study of the effect of the bending modulus $\kappa_{CGP}$ on the actin force $f_A$ estimated from experiments. The CGP forces were generated from the hyperbolic tangent transition from Eq. 11 with $\gamma = 0.1$ and $s_0 = 46$ nm.

(b) **Transition Radius.** We treated the transition radius $s_0$ of the preferred curvature of the CGP as a fitting parameter when estimating the total actin force. The transition radius was approximately equal to the radius where the first derivative of the force $f_W + P_0$ was maximized, which resulted in a transition radius of $s_0 = 46$ nm. In Fig. S9, actin forces with transition radii of $s_0 = 36$, 46, and 56 nm are compared to highlight the effect of this parameter. Selecting a transition radius larger or smaller than $s_0 = 46$ nm results in enhanced spatial fluctuations in the actin force density. In addition, Table S5 shows that the changes

TABLE S5: Effect of CGP parameters on the total required actin force $F_A$ and the endocytic width $R_W$. $F_A$ is calculated by integrating the force $f_A$ from $r = 0$ to $R_W$. $R_W$ is defined as the location where the experimentally estimated actin force $f_A = 0$.

| Study | Parameter | $F_A$ [pN] | $R_W$ [nm] |
|---|---|---|---|
| 4a | $\kappa_{CGP} = 20\,k_BT$ | 3100 | 48 |
| | $\kappa_{CGP} = 285\,k_BT$ | 2800 | 48 |
| | $\kappa_{CGP} = 500\,k_BT$ | 2600 | 51 |
| 4b | $s_0 = 36$ nm | 3000 | 48 |
| | $s_0 = 46$ nm | 2800 | 48 |
| | $s_0 = 56$ nm | 3000 | 46 |
| 4c | $H_0 = 36$ nm$^{-1}$ | 2900 | 48 |
| | $H_0 = 46$ nm$^{-1}$ | 2800 | 48 |
| | $H_0 = 56$ nm$^{-1}$ | 2700 | 49 |

in transition radius have a minimal effect on both $F_A$ and $R_W$. However, our chosen value minimizes the required force $F_A$. Thus we feel that this choice of transition radius makes physical sense.

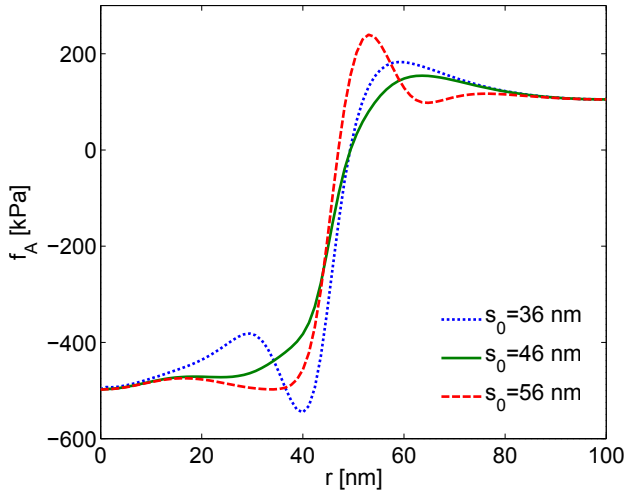


FIG. S9: Study of the effect of center of the transition radius $s_0$ of the CGP on the experimentally estimated actin force $f_A$. The CGP forces were generated from the hyperbolic tangent transition from Eq. 11 with $\gamma = 0.1$.

(c) **Preferred Curvature.** We also considered the effect on the actin force of changing the preferred curvature $H_0$ of the CGP. We observed the effect of a selected range of preferred curvatures ($H_0 = 0.016$, 0.02, and 0.024 nm$^{-1}$) on the estimated actin force. We found that for this range, the change in shape of the actin force was minimal. In addition, Table S5 shows that the changes in preferred curvature have a minimum effect on both $F_A$ and $R_W$.

(d) **Alternative CGP Patch Transition.** Finally, an alternative approach to modeling the transition of the CGP patch is to vary the preferred curvature and keep the bending modulus constant. The CGP forces are then defined by

$$f_{CGP}(s) = \frac{1}{2r}\frac{\partial}{\partial s}\left(r\frac{\partial}{\partial s}\left(-2\kappa_{CGP}H_C(s)\right)\right), \tag{S6}$$

where $H_C$ is preferred curvature of the CGP proteins. The preferred curvature is modeled with the tanh

function:

$$H_C(s) = \frac{H_0}{2}\Big[1 - \tanh\left[\gamma(s - s_0)\right]\Big], \tag{S7}$$

where $H_0$ is the maximum preferred curvature. When the CGP forces are calculated using Eqs. S6 and S7 for the same baseline parameters, the resulting actin force is nearly identical to the baseline case which uses Eq. 11. Using the transition curvature in Eqs. S6 and S7 results in a pulling force and endocytic width of $F_A = 2800$ pN and $R_W = 48$ nm, respectively.